# Chapter 4

## Solvent Vapor Assisted Self-Assembly of Semiconducting Polymers at the Air-Liquid Interface: Impact on Nanoscale Morphology and Optoelectrical Anisotropy

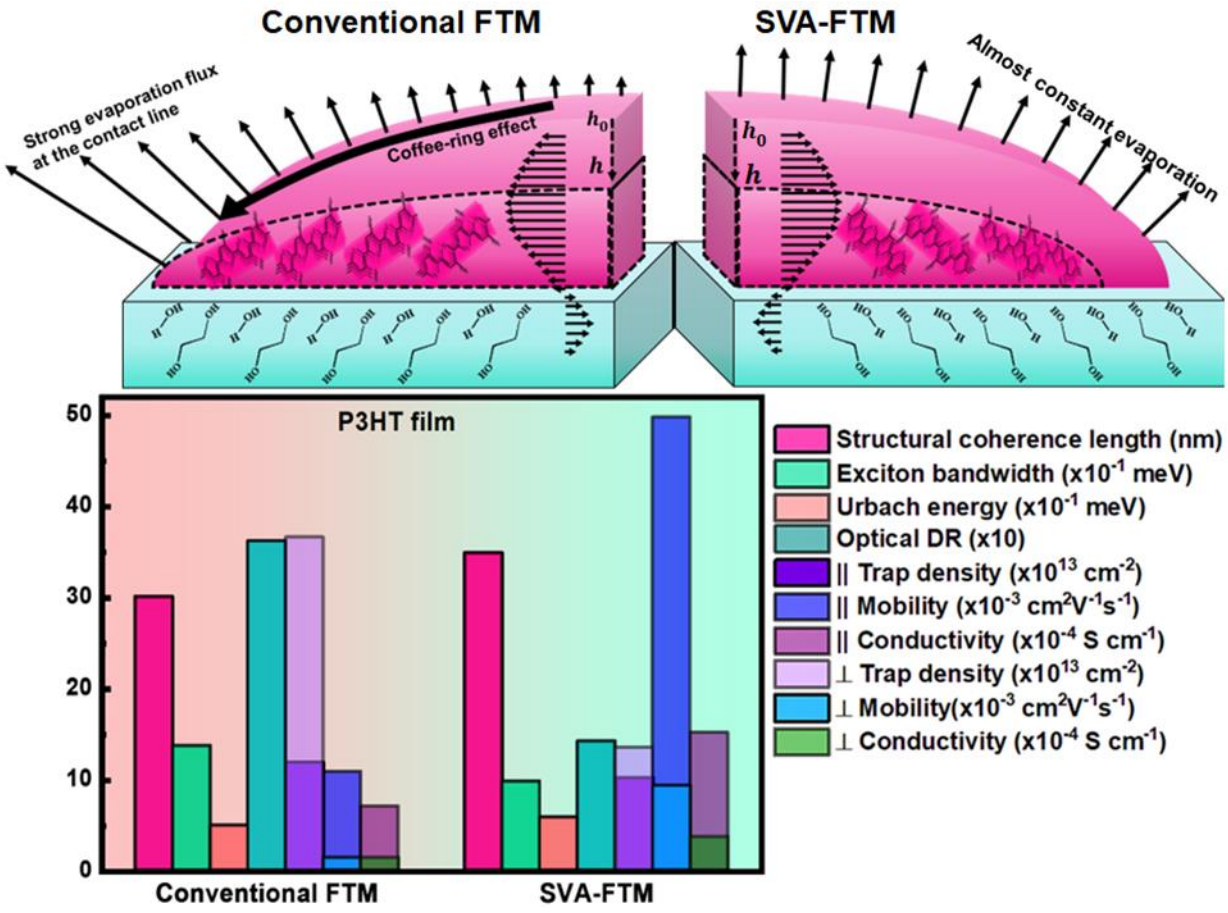

## 4.1.Introduction

Organic semiconducting polymers (OSPs) have received huge scientific interest owing to their striking features of low-cost solution-processing compatibility, easy functionalization, and mechanical flexibility [57,117]. However, the performance of OSP-based electronic devices is limited by inferior charge transport properties, short operational lifetime, and reproducibility issues.[48,82] In general, charge transport within the crystalline domains occurs through the conjugated polymer backbone assisted by interchain hopping through overlapped π-electron clouds between adjacent polymeric molecules [75,82]. Thus, besides the development of high-mobility OSPs, efforts have been made to utilize process advantages that can reduce grain boundaries by long-range molecular ordering. Now, two facets exist in solving such issues: one is understanding the mechanism behind such poor device performance through exploring fundamental properties and then utilizing the knowledge to improve the film microstructure and molecular orientation. Besides mobility and crystallinity, anisotropic charge transport due to uniaxial molecular orientation is another fundamental property that helps to delineate the relationship between long-range molecular ordering and macroscopic properties of the devices [57]. Various approaches have been explored to enhance the degree of crystallinity, molecular orientation, and packing modes of the active semiconducting layer by optimizing molecular self-organization. However, nonuniform solvent evaporation and three-dimensional crystal growth due to π-π interaction make the self-organization process challenging to control.

Amongst commonly used methods, spin coating and drop casting yield nonuniform films, [118] especially material wastage is huge in the spin coating method. There also exist several alternating methods to control crystallinity and orientation, like solution shearing, [117] blade-coating [117], inkjet printing, [119] dip-coating, [117] directional epitaxial

solidification, [54,102] slot die coating, [120] spray coating, [121] etc. Researchers also tried many pre- and post-processing methods like nanofiber formation, [31] solvent vapor annealing, [122] electric field annealing, [123] etc., to enhance the crystallinity. Our group has also developed a facile and low-cost film fabrication technique named "*floating-film transfer method* (FTM)", [57] which yields a large area [67] and uniaxially oriented thin polymeric film. However, similar to other methods, nonuniform solvent evaporation in FTM, along with the high degree of conformational freedom, causes many cumulative and non-cumulative lattice disorders, which limits the oriented domain size and disrupts the molecular-wavefunction overlap [124]. The use of solvent vapor is one of the solutions to overcome this issue, and there are few reports regarding this, like, Deepak et al. used directional solvent vapor annealing (DSVA) to align pentacene (TIPS-PEN), [125] Jung et al. used different solvent vapor to crystallize TIPS-PEN, [126] Paul et al. used THF vapor to heal P3HT composites, [127] Hao et al. used solvent vapor assisted spin coating [128]. However, none achieved anisotropic charge transport in OSPs with high mobility, as post-processing cannot orient polymer backbones, and it can also deteriorate organic gate dielectrics, which is not suitable for low-power transistor applications. Thus, a unified approach is needed, which can yield homogeneous, uniaxially orientated thin films with a highly crystalline order, and by transferring the pre-fabricated solid thin film onto desired substrates, we can fabricate high-performance organic electronic devices like OFETs.

In this present work, we propose an integrated solution linking the key advantages of conventional FTM and the effect of solvent vapor treatment and to demonstrate this method, we have opted one of the most studied OSP, regioregular poly(3-hexylthiophene-2,5-diyl) (rr-P3HT), as shown in Figure 4.1 (a). In FTM, fast evaporation of low boiling point solvents like chloroform (dynamic-FTM) limits the time for molecular self-organization during the film formation over a hydrophilic liquid substrate bed. The use of

high boiling point solvents like chlorobenzene (static-FTM) could be a solution for this, but it is well-documented that static-FTM is unable to improve planar anisotropic charge transport properties compared to the dynamic one [85]. In our newly developed approach, named solvent vapor assisted FTM (SVA-FTM), a solvent vapor saturated environment manipulates both evaporation behaviour as well as solution spreading dynamics that facilitate the formation of a highly crystalline film having long-range molecular ordering. To investigate the impact on nanoscale morphology and optoelectrical anisotropy, as-prepared films were thoroughly studied using atomic force microscopy (AFM), Kelvin probe force microscopy (KPFM), thin-film X-ray diffraction (XRD), high-resolution transmission electron microscopy (HR-TEM), polarized UV-vis spectroscopy, Raman spectroscopy and cyclic voltammetry (CV). Furthermore, parallel and perpendicular organic field-effect transistors (OFETs) were fabricated and used to evaluate the anisotropic charge transport properties. All these results established an elegant way to precisely control the crystallinity and molecular ordering in OSPs for high-performing OFETs and provide an insight into the fundamentals of structure-property correlation and the reason for improved charge transport.

## 4.2.Results and Discussion

### 4.2.1. Film formation mechanism

In FTM, a gradient in surface tension causes low surface energy solutions to spread over the high surface energy liquids, and this natural spreading is governed by the spreading coefficient, [70,124] $S$ ($= \gamma_{liq-air} - \gamma_{sol-air} - \gamma_{liq-sol}$ ; $\gamma$ : surface tension). Various viscoelastic flows like thermocapillary flow, diffusocapillary flow, coffee-ring effect, tangential pressure gradient driven flow, and compressive viscous flow are associated with this spontaneous spreading and solvent evaporation process [98,124]. Additionally,

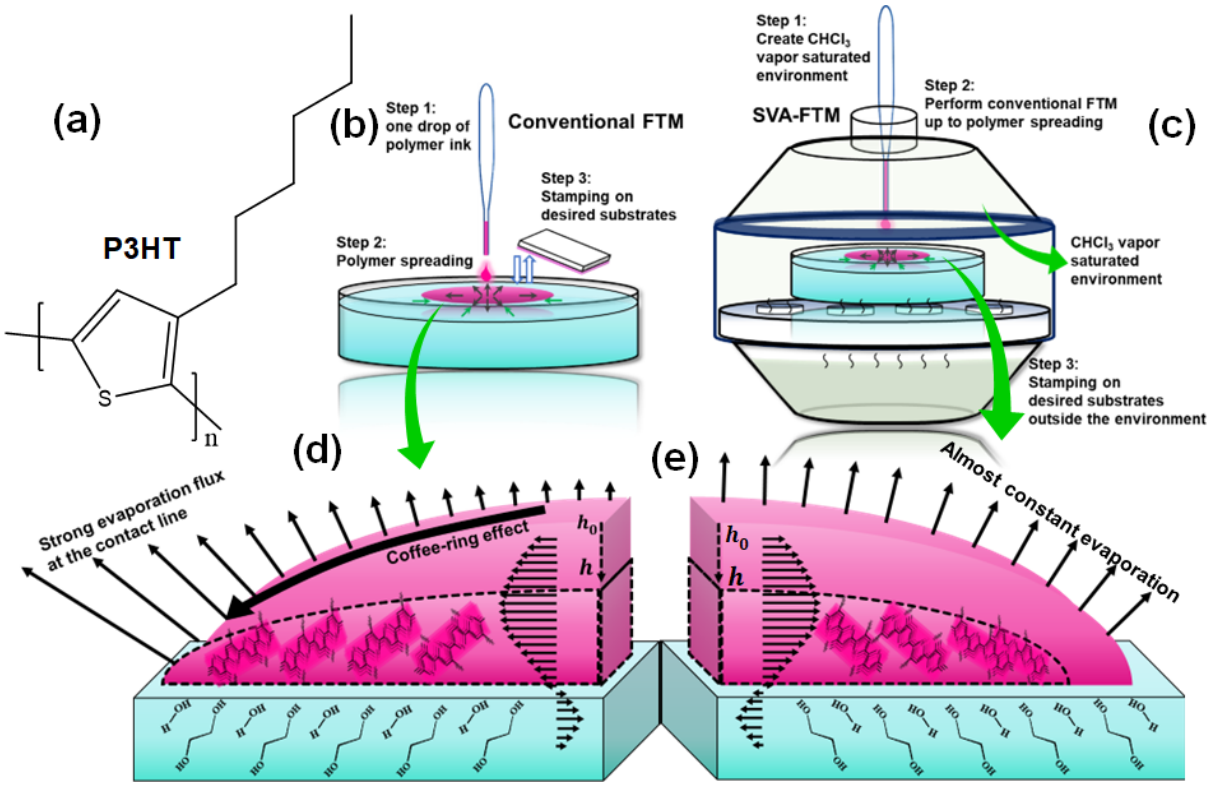


**Figure 4.1** (a) P3HT molecular structure, Schematic representation of conventional FTM (b) and SVA-FTM (c), and the mechanism of evaporation has been shown in both conventional (d) and solvent vapor assisted case (e).

conformational changes in flexible P3HT backbone and intermolecular π-π interactions govern the microstructural evolution in P3HT thin films. As reported by us previously, [124] the formation of edge-on type molecular stacking in solid OSP thin film occurs mainly because of the interplay between resistive viscous force, the elasticity of the air-solution interface, and progressing tangential pressure gradient-driven flow. The semiconducting polymer lamellae in outward progressing thin liquid film face two constraints in their path: the elastic air-solution interface and the resistive viscous force at the solution-liquid interface, which facilitates the self-assembly of fish-bone-like backbones in an 'edge-on' type arrangement. Nevertheless, other capillary flows, along with the Marangoni flow inside the radially progressing thin liquid film cause many lattice disorders even within the crystalline domains of P3HT macromolecules. Thus, in the

following section, we have explained the critical role of solvent evaporation on the self-assembly of OSP molecules at the air-liquid interface.

When a drop of low concentration (10 mg/ml) and properly dis-entangled (utilizing thermal energy) chloroform solution of OSPs, falls upon a hydrophilic liquid bed, interfacial surface tension gradient drives the spreading of the solution. During this spreading, the solvent evaporates from the solution very rapidly because of the high molecular energy or high vapor pressure of chloroform (200 mm Hg at 298K). Since quasi-steady evaporation is a diffusion-limited process, the evaporation flux ($J_s$) strongly depends on the vapor transfer rate through the solution-vapor interface as well as the vapor concentration in the atmosphere [129,130]. For evaporation in an open-air environment, $J_s$ is strongly divergent towards the air-liquid-solution triple contact line and minimum at the apex for contact angle, $0° < \theta_{ca} < 90°$, [97] as schematically shown in Figure 4.1 (d). Moreover, due to continuous depinning of the triple contact line during spreading and evaporation, uncertainty in $\theta_{ca}$ is higher for chloroform solution [97]. This causes many flow instabilities inside the polymer solution, which introduces many microstructural defects and limits the coherence length, and momentarily, trap states become 'frozen' inside the dried thin films. However, if we saturate the immediate environment with solvent vapor, $J_s$ will be constant (Figure 4.1 (e)) and according to Kenneth et. al., [131] Marangoni instability will not be there to hinder the self-assembly process for a slowly evaporating drop. Thus, a more thermodynamically stable conformation can be achieved in this case which will help enlarge the oriented domain size.

### 4.2.2. Thin film characterizations

At first, to probe the effect of solvent vapor on as-prepared FTM films, the surface texture of both the conventional-FTM and SVA-FTM fabricated thin films was investigated

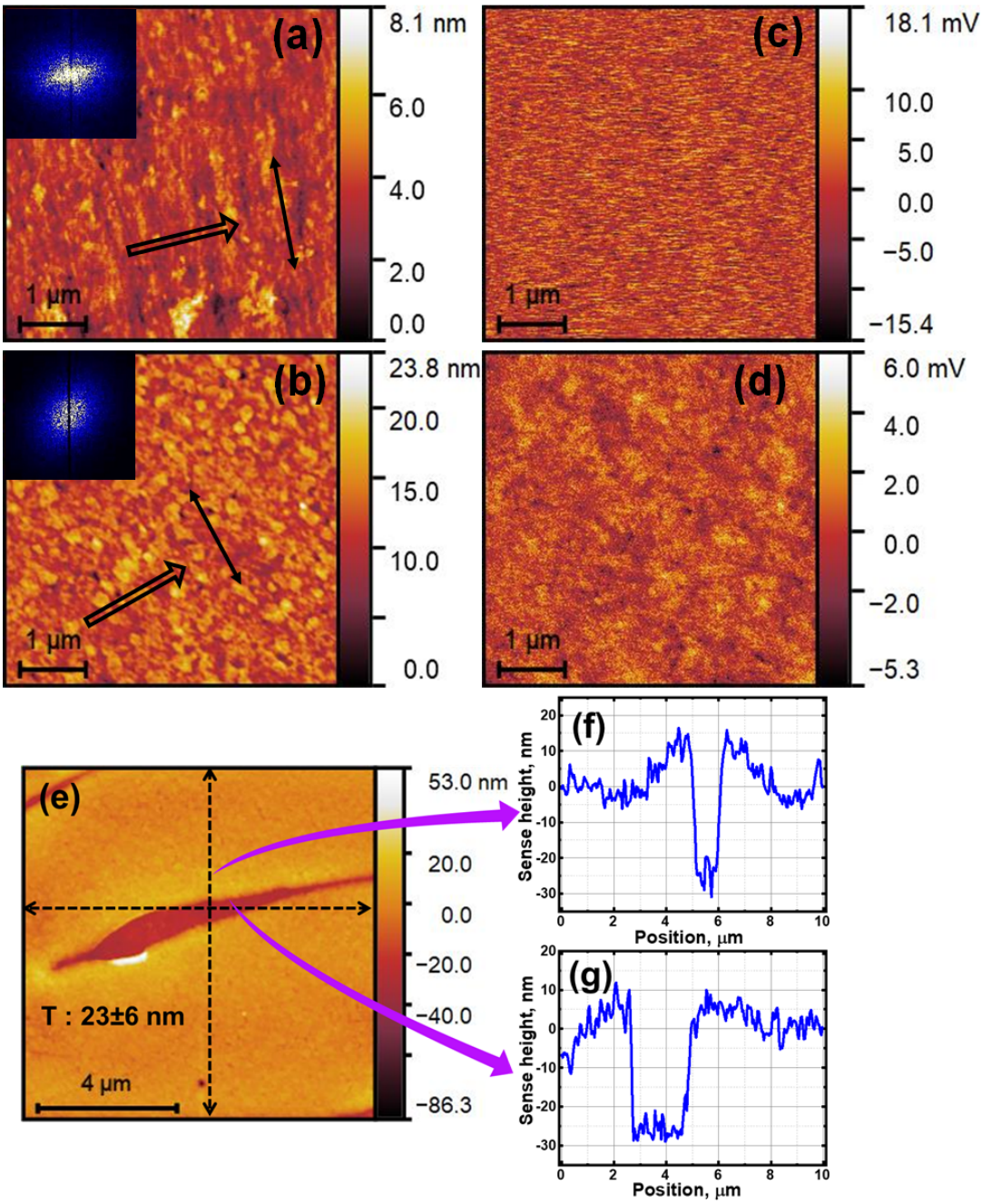


**Figure 4.2** AFM height profile for conventional FTM films (a) and SVA-FTM films (b), respectively. The black arrows in the AFM images indicate the molecular orientation (double arrow) and film progression direction (single arrow) in FTM films. (c) and (d) describes the work function mapping for the conventional and SVA-FTM films, respectively. Next, (e) shows AFM step-height scan for SVA-FTM film and corresponding height profile along horizontal (f) and vertical (g) direction.

through AFM (in tapping mode) and KPFM, as shown in Figure 4.2. The 3D roughness topography and work function mapping were recorded at room temperature in the same 4×4 $\mu m^2$ area. The 2D fast Fourier transform (FFT) of the roughness profile, shown in

Figure 4.2 (a) & (b) inset, evidenced the clear isotropic nature of the surface roughness. After that, the root mean square roughness ($\boldsymbol{R_{rms}}$) or interface width, which is the reflection of the inner-microstructure of the films, has been estimated using the Gwyddion software. The $\boldsymbol{R_{rms}}$ for conventional-FTM films is found to be 0.86 nm, while it is around 2.15 nm for SVA-FTM films. It suggests that the chloroform environment-induced slow evaporation helps the smooth dis-entanglement of P3HT chains and enhances the degree of molecular stacking, increasing the overall surface roughness. Next, measuring the local contact potential difference ($V_{CPD}$) at each point of the scan area (356×356 pixel), the work function topography of the FTM films has been reconstructed through KPFM in amplitude modulation (AM) mode [106]. The electrostatic interaction between the FTM film surface and the conducting Pt-coated Si tip pictures the processing-induced topographical evolution of work function almost in real-time (Figure 4.2 (c & d)). The normalized probability density functions related to $V_{CPD}$ have been fitted with a Gaussian function and found that the r.m.s. $V_{CPD}$ for SVA-FTM films is much lower, 1.2 mV, compared to 3.9 mV for the conventional one. As the average work function of film surfaces controls the charge delocalization from the semiconducting layer to the metal contacts, lower the local $V_{CPD}$, easier will be charge injection and collection through the metal-semiconductor interface.

After the surface studies, molecular stacking and film crystallinity was studied through the meridional XRD scan, as shown in Figure 4.3 (b). For both films, a series of (*h*00) diffraction peaks in a monoclinic lattice system [54] have been observed along $q_z$-axis, i.e., the alkyl side-chain stacking lies perpendicular to the substrate surface. As per our previous observations as well as other reports, [57,124,132] OSP films prepared through FTM usually take 'edge-on' type orientation. Nonetheless, a chloroform vapor saturated environment provides the required crystallization time and eventually predominantly

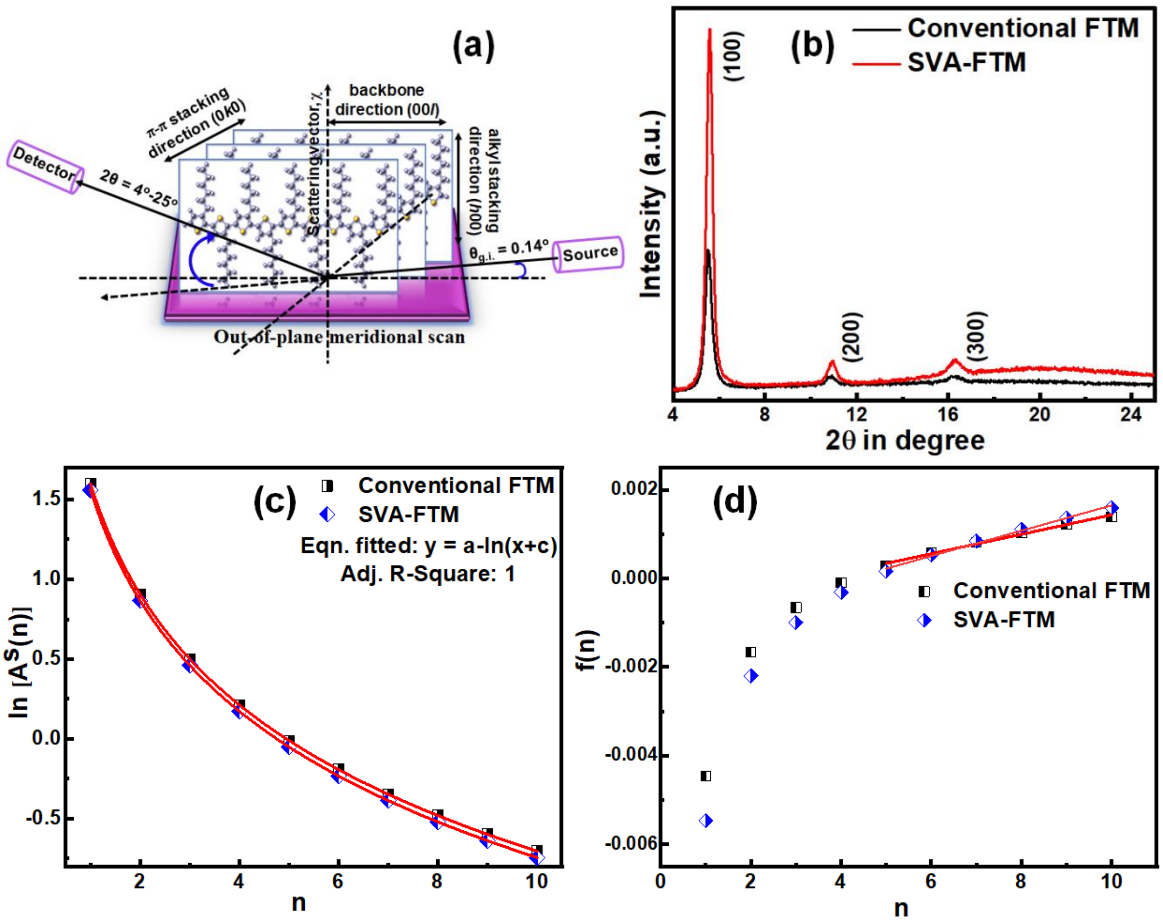


**Figure 4.3** (a) Out-of-plane XRD has been schematically shown, (b) Out-of-plane XRD pattern for both conventional and SVA-FTM films, (c) shows the $\ln[A^s(n)]$ $vs$ $n$ plot which gives $M$ value and (d) represents the $f(n)$ $vs$ $n$ plot which yields $g$ and $e_{rms}$.

affects the molecular orientation and overall crystallinity of P3HT films. It can be clearly seen by comparing the diffraction peak intensity and full width at half maximum (FWHM) of the (100) peak. Although for a structurally broadened profile, the FWHM ($\beta$) has been first corrected using the following relation, [133]

$$\beta = \sqrt{\left[\sqrt{{\beta_h}^2 - {\beta_g}^2}\right]\left[\beta_h - \beta_g\right]} \tag{4.4}$$

Where $\beta_h$ and $\beta_g$ represent the experimentally observed FWHM and instrumental broadening (calculated from the NIST Si standard). Next, the average coherence length along the $q_z$-axis, has been calculated using the Debye-Scherrer formula and tabulated in

TABLE 4.1. The interlamellar spacing, $d_{h00}$ also reduced 0.2 Å in the case of SVA-FTM films, and the average no. of Bragg's plane stacked together, which diffract coherently, is found to be 19 and 22 for conventional-FTM and SVA-FTM films, respectively. Thus, a higher degree of crystallinity for slow evaporation-induced films should ease charge delocalization to a greater extent overwhelming the grain boundary effect. In P3HT semicrystals, where amorphous and crystalline domains coexist, the charge transport is dominated by the orbital overlap in the crystalline domains containing ordered molecular packing. Thus, to get an insight into the microcrystalline domains and local molecular orientation, we have decoupled size-related broadening from cumulative disorder using the Warren-Averbach (W-A) approach, [84,88,134] as described in section 3.2.2. Thus, from the logarithmic fitting of $\ln[A^s(n)]$ $vs$ $n$ plot, we estimated the effective mean coherence length, $M$, and from the $f(n)$ $vs$ $n$ plot, we estimated the average value of $g$ and $e_{rms}$ (Figure 4.3 (c) & (d)). However, improper background determination in higher-order diffraction peak tails often causes errors in lowest-order Fourier coefficients, [88] which momentarily leads to the 'hook effect' (i.e., negative $f(n)$). Because of this 'hook effect' lowest-order coefficients up to $n = 4$ have been ignored, and a linear fit beyond these yields $g$ and $e_{rms}$. Thus, from W-A diffraction peak shape analysis, we found that degree of paracrystallinity and statistical instability in lattice parameters within the crystalline

**TABLE 4.1** Findings of XRD peak shape analysis.

| **Sample** | **Average $d_{h00}$ in nm** | **Alkyl stacking coherence length** | | $g(\%)$ | $e_{rms}(\%)$ |
|---|---|---|---|---|---|
| | | **W-A graphical, M (nm)** | **Scherrer, $L_c$ (100) in nm** | | |
| Conventional FTM film | 1.62 | 19.8 | 30.1 | 2.75±0.17 | 1.48±0.05 |
| SVA-FTM film | 1.60 | 22.1 | 34.9 | 3.48±0.19 | 1.69±0.06 |

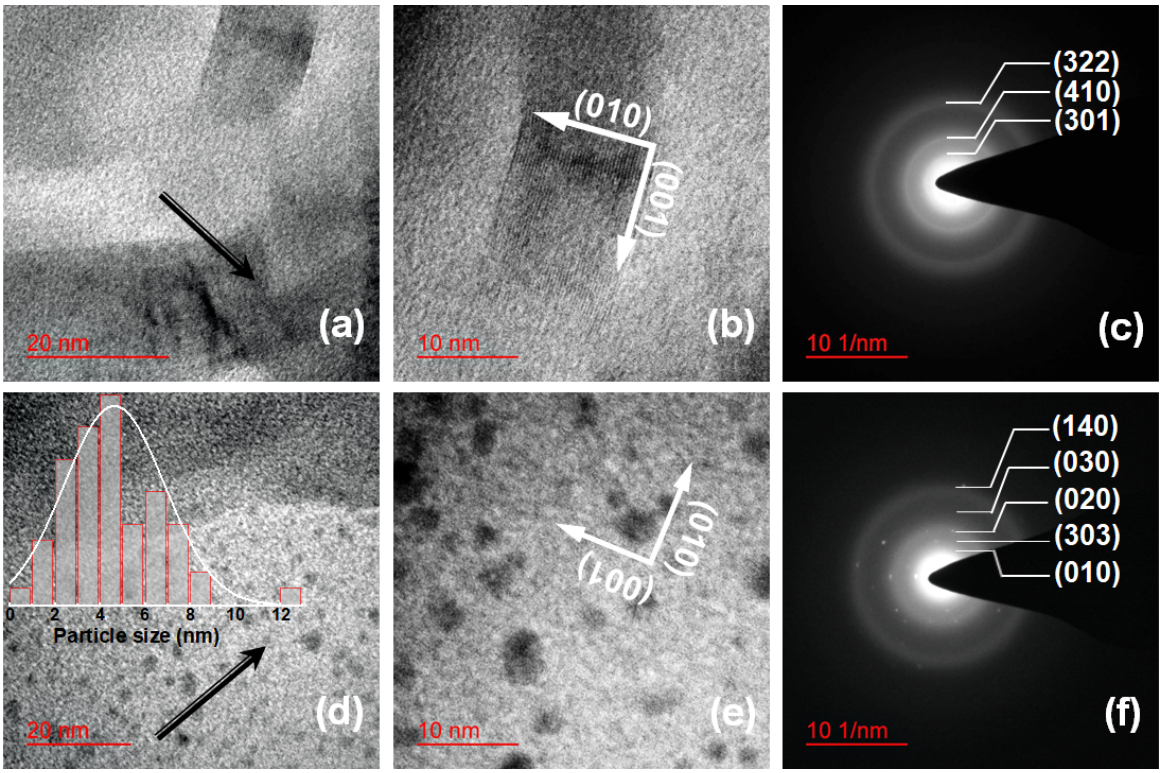


**Figure 4.4** Bright field HR-TEM images and respective SAED patterns for conventional FTM films (a-c) and SVA-FTM films (d-f), respectively. The film progression direction in FTM films has been shown by single arrow in black.

domains is higher for SVA-FTM films (3.48% and 1.69%) as compared to conventional-FTM films (2.75% and 1.48%). This can be explained as, during the growth of semicrystals in the conventional case, rapid evaporation of chloroform arrests the 'edge-on' type molecular packing into a dried state, having a long viscoelastic relaxation time. On the other hand, solvent vapor-assisted slow evaporation offers temporal autonomy to attain a thermodynamically more stable aggregated packing. Thus, SVA-FTM helps to grow the size of ordered crystalline domains and causes the formation of smaller microcrystals, enhancing the overall paracrystallinity. A higher degree of interdigitation along the $q_z$-axis also contributes to the cumulative disorder. Nevertheless, higher coherence length and shorter interlamellar spacing for SVA-FTM P3HT films should provide a low resistive route for charge transport owing to a higher degree of molecular wave function overlap.

After macroscopic investigations of the crystalline domains through XRD, we go further at a sub-micrometer level to probe the local molecular orientation and nanomorphology of the FTM films using HR-TEM. The effect of solvent vapor on FTM films can be directly visualized in the bright-field (BF) HR-TEM images by optimizing the measuring conditions like irradiation level, objective aperture size, and tilt-angle of the single-tilt holder, etc. that minimizes polymer damage and provide better images. In Figure 4.4 (a-b) & (d-e), clear phase contrast can be seen in both films, which are not originated from any topographical feature of the film surface or any type of staining. According to M. Brinkmann et al., [54,102] they must have originated from different crystalline packing of polymer chains as ordered crystalline domains and amorphous zones show different viscoelastic responses. In oriented crystalline regions, the degree of electron diffraction is much higher because of the high scattering factor compared to amorphous zones. Now, while imaging through TEM, an objective aperture is normally used to cut off most diffracted electrons, and thus crystalline domains appear dark while non-diffracting amorphous zones look brighter. In the case of SVA-FTM films, small dot-like crystalline regions can be seen, which have a size distribution within 13 nm and an average size of 4-5 nm. This is a unique quantum dot-like morphology of P3HT, distributed over semicrystalline as well as amorphous zones. At a little higher magnification (×250K), keeping the electron beam parallel to the polymer backbone orientation, highly ordered domains can be visualized for both cases. However, for conventional FTM, the ordered crystalline domains aligned perpendicular to the flow direction are separated by amorphous zones. In contrast, for SVA-FTM, quantum dot-like polymer aggregates are bridging the neighboring semicrystals, and thus a better electron delocalization through a low resistive path can be expected for SVA-FTM films. Next, within the ordered domains, a periodic Z-contrast variation with periodicity 3.7±0.1 Å for conventional ones and 3.5±0.2 Å for SVA-

FTM films suggests that 'edge-on' stacking dominates the film microstructures. In Figure 4.4 (c & f), selected area electron diffraction (SAED) patterns are shown, where concentric Scherrer rings in reciprocal lattice represent the amorphous nature of both films. However, some dot patterns support comparatively higher crystallinity of the aggregated nanostructures in SVA-FTM films, as they possess a higher scattering factor.

Further, to get an insight into the evolution in electronic band structure due to solvent vapor-assisted nanostructuration of crystalline lamellae, we have investigated both films deposited over quartz glass through a non-polarized UV-vis spectroscopy at 300 K. As shown in Figure 4.5 (a), P3HT films prepared through the conventional route shows the absorption maxima ($\lambda_{max}$) at 538 nm, along with a less evident vibronic shoulder at 595 nm. While in the case of SVA-FTM films, there can be seen a well-structured absorption profile having two distinct absorption peaks located at 552 nm ($\lambda_{max}$) and 600 nm, along with a bathochromic spectral shift of the absorption band-edge. A pronounced vibronic shoulder indicates the presence of an extended π-conjugation and more ordered P3HT backbones [70,132]. After that, to characterize the aggregation type, we have used the weakly interacting H-aggregate model developed by F. C. Spano [135,136]. According to this model, the absorption intensity ratio, $R_{abs}(= A_{0-0}/A_{0-1})$ <1 for H-type aggregates and >1 for J- aggregates. For SVA-FTM films, $R_{abs}$~0.70 is a clear indication of H-aggregation, which was expected because solvent vapor-assisted intermolecular interaction occurs during the evolution of 'edge-on' orientation of P3HT backbones perpendicular to the flow direction. Now, in H-type domains, due to interband mixing, $R_{abs}$ is related to the free-exciton bandwidth ($W$), and the main intramolecular vibration energy ($\hbar\omega_p$). Thus, taking the Huang-Rhys factor to be unity, $R_{abs}$ can be expressed as

$$R_{abs} = \left(\frac{1-0.24W/\hbar\omega_p}{1+0.073W/\hbar\omega_p}\right)^2 \quad (4.5)$$

Here, $W$ corresponds to the interchain Coulombic coupling ($J_0$) between proximate molecules as $W = 4J_0$ and thus, the lower the value of $W$, i.e., excitonic coupling, the higher will be the effective conjugation length. The value of $W$ estimated for conventional- and SVA-FTM films are 137 meV and 98 meV, respectively, and thus a better electronic coupling is envisioned for SVA-FTM films. The energy corresponding to the photo-induced lowest electronic transition ($E_g$) is estimated using the Tauc relation, [124] and $E_g$ is found to be 1.98 eV and 1.95 eV for Conventional FTM films and SVA-FTM films, respectively, as shown in Figure 4.5 (a). Again, slow evaporation-induced nanostructuration and many small microcrystal formations can introduce static disorders as well as other microscopic perturbations, which causes the quantum mechanical penetration of localized states into the optical gap. To study this, absorption line shape at the low-energy region has been analyzed using the Urbach rule, [93,112,113] equation 3.4. Thus, from the $\ln(\alpha)\ vs\ \hbar\omega$ plot (Figure 4.5 (b)), Urbach tail-width, $E_U$ ($= K_B T/\sigma_T$) is found to be higher (~58.7±0.2 meV) for SVA-FTM films as compared to the conventional one (~49.4±0.1 meV). Thus, the deeper exponential tailing of the localized density of states into the forbidden optical gap in the case of SVA-FTM films tallies the results from the XRD line-shape analysis.

Now, previous reports [57] suggest that P3HT films self-assembled at the air-liquid interface are usually found to contain uniaxially oriented domains. Thus, we have recorded the polarised electronic absorption spectra to examine the degree of molecular orientation present in both films at a macroscopic level. From the perusal of Figure 4.5 (c), it is clearly evidenced that both films show optical anisotropy, where maximum absorption is found perpendicular to the film spreading direction. As the transition dipole moment corresponding to the 0-0 transition lies along the P3HT backbone due to the highest electron

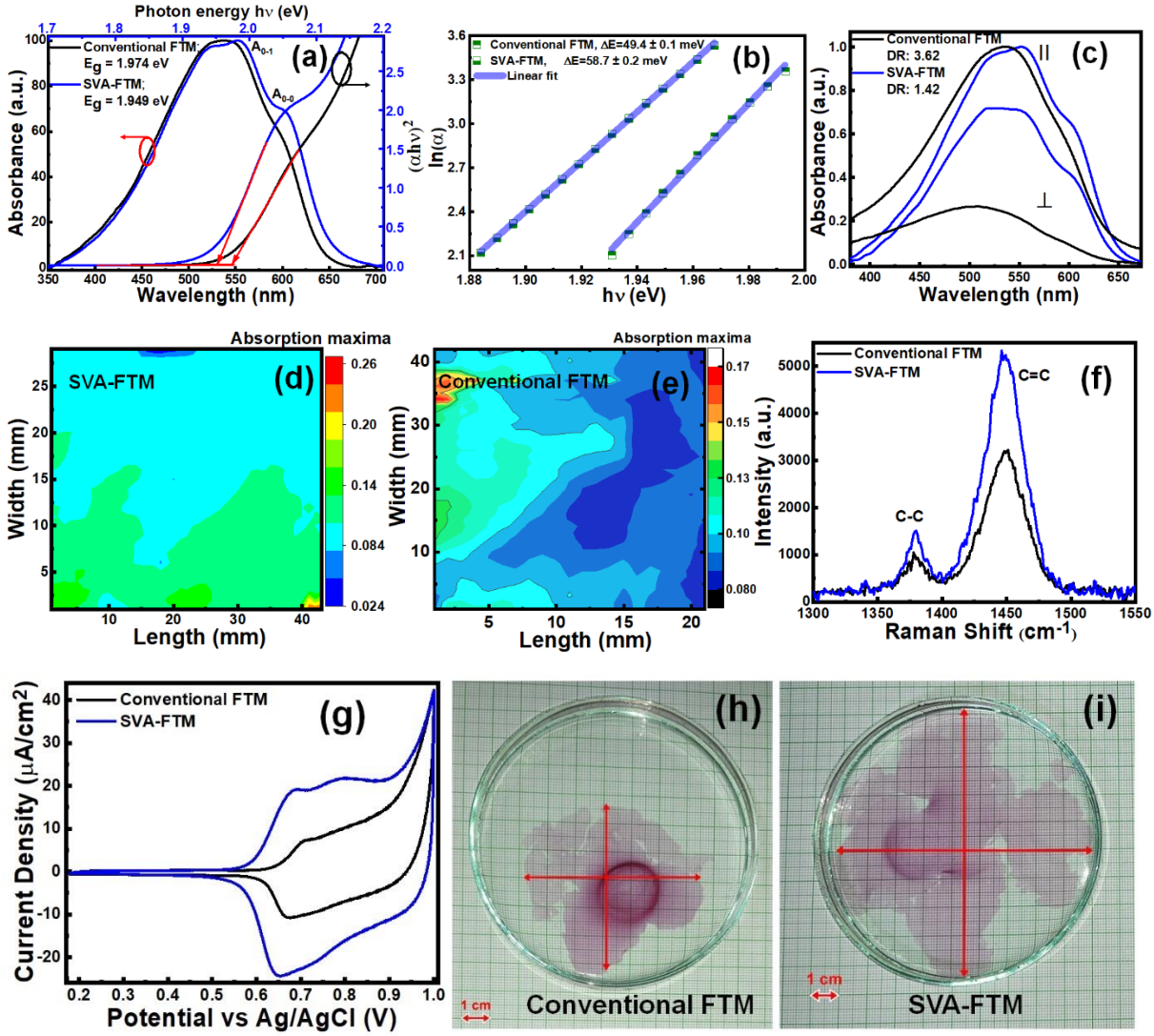


**Figure 4.5** (a) shows non-polarised optical absorption spectra, (b) Urbach plot, (c) polarised optical absorption spectra, (f) Raman spectra, (g) cyclic voltammetry measurement for conventional and SVA-FTM films, (h) & (i) are the real images of P3HT films, and (d) & (e) represents 2D distribution of absorption maxima (or thickness) in SVA-FTM film and conventional-FTM film, respectively.

density, thus, linearly polarized optical absorption will be highest when the polarization of light is parallel to the P3HT backbone orientation [75]. So, we can conclude that P3HT molecules are oriented perpendicular to the film spreading direction while assembling over a hydrophilic liquid bed. Now, the average dichroic ratio (***DR***) was found to be ~ 3.63 and ~ 1.42 for conventional FTM and SVA-FTM films, respectively, which are in accordance with the HR-TEM results. The decrease in ***DR*** for SVA-FTM films can be explained as

slow evaporation in a chloroform vapor saturated environment causes the polymer solutions to spread slower compared to the conventional case. In the normal air environment, rapid evaporation from the triple contact line originates a radially outward flow related to the 'coffee-ring' effect along with a thermocapillary flow, [124] which enhances the overall spreading speed of the solution, and thus the tangential compressive viscous force helps more P3HT backbones to orient perpendicular to the flow direction. For solution-processed thin films spread over a few $cm^2$ areas, inhomogeneity in film thickness is one of the key hindrances to poor reproducibility in organic semiconducting polymer-based devices. Thus, we have characterized the P3HT films through an in-house developed 2D positional mapping system to study the thickness variation in our newly developed SVA-FTM films. The real images of both as-prepared P3HT FTM films are shown in Figures 4.5 (h) & (i). These P3HT thin films coated on quartz substrates (stamped almost 1/3 of the entire film area) were irradiated with a fixed incident beam, and the whole absorption spectra transmitted through the sample were simultaneously recorded by a multichannel detector (PMA, 7473-36, Hamamatsu Photonics). These position-dependent absorption spectra were recorded in a scan area of 29×43 $mm^2$ for SVA-FTM and 42×22 $mm^2$ in conventional-FTM film, in a step of 0.5 mm, using a computer-controlled X–Y mobile stage. As shown in Figure 4.5 (d), a uniform thickness distribution can be seen in most of the film area except for the two-extremum case, the apex and end of the film, due to the apparent film growth mechanism.[124] However, the conventional film shows more thickness variation, as seen in Figure 4.5 (e). Thus, SVA-FTM films can be used as a suitable active layer for fabricating different organic electronic devices.

Next, the possible change in the vibrational modes due to aggregated nanostructure formation, Raman spectrum was also recorded, and for comparison purposes, all the parameters like temperature (300K), laser power, spot size, grating (1200 grooves/mm) and

**TABLE 4.2** Findings of Raman peak analysis.

| **Conventional FTM film** | | | |
|---|---|---|---|
| **Peak position ($cm^{-1}$)** | **FWHM ($cm^{-1}$)** | **Peak assigned** | **Area under the curve** |
| 1380.0 | 22.2 | C–C skeleton stretch | 17193 |
| 1448.3 | 37.3 | C=C symmetric stretch | 114449 |
| **SVA-FTM film** | | | |
| 1379.9 | 19.6 | C–C skeleton stretch | 24930.8 |
| 1448.0 | 36.1 | C=C symmetric stretch | 190784.5 |

step size (1.2 $cm^{-1}$) were kept constant for both films. As shown in Figure 4.5 (f), the Raman spectrum of both films shows the two characteristic peaks of rr-P3HT corresponding to the vibration modes related to C=C symmetric stretch (~1448 $cm^{-1}$) and C–C skeleton stretch (~1380 $cm^{-1}$), respectively. It is evident that the peak positions for both cases are almost the same, while the Raman intensity (and area under the curve as well) for SVA-FTM films is almost 1.5 times higher as compared to conventional-FTM films. This increase in Raman intensity, i.e., transition probability corresponding to particular Raman active modes, can be attributed to the longer coherence length in SVA-FTM films. Moreover, the FWHM of Raman peaks is found to be decreased in SVA-FTM films for both the vibrational modes (TABLE 4.2), which is a clear indication of extended and more compact π-orbital overlap in SVA-FTM films [137].

In order to study the evolution of the highest occupied molecular orbital (HOMO) position in both P3HT films having different microstructures, cyclic voltammetry (CV) measurement has been carried out using a standard three-electrode system and non-aqueous electrolyte (0.1 M Tetrabutyl ammonium perchlorate (TBAP) in acetonitrile). P3HT films transferred over pre-patterned ITO substrates with a conducting geometrical area of 0.5×0.5 $cm^2$ were used as working electrodes, $Ag/Ag^+$ as reference, and coiled Platinum wire as a counter. After purging highly pure $N_2$ gas for 15 minutes into the electrolyte, the working

electrodes were dipped into it for 6 minutes each, and 10 CV cycles were run to stabilize the system before performing the experiments. In a dark environment (as P3HT is a photosensitive polymer), CV scans were recorded in the range of 0.18 V to 1.00 V (vs. Ag/AgCl) in the step of 1 mV, keeping a fixed scan rate of 50 mV/s. It can be seen in Figure 4.5 (g) that overall CV current was increased ~2.5 times in SVA-FTM films with a ~49.3 mV shifting of oxidation onset ($E_{ox}$) towards the lower side. The enhancement in CV current in films having an almost similar thickness may arise due to the high surface roughness in SVA-FTM films. Now, the HOMO positions from oxidation onset have been evaluated for both P3HT films by taking ferrocene reference, $E_{1/2(ferrocene)} = 0.405V$ and applying the standard equation, [79]

$$E_{HOMO} = \left[\left(E_{ox} - E_{1/2(ferrocene)}\right) + 4.8\right] eV \tag{4.6}$$

Thus, the shifting of oxidation onset ($E_{ox}$) to lower potential side (~49.3 mV) can arise due to two facts: one, the surface roughness of the as-prepared films, as electron removal from the peaks of rough surfaces are easier through the electrolyte, and secondly, the raising of HOMO position due to a more ordered P3HT chain. However, as studied by Denis et. al., [138] roughness of the working electrode can only affect the shape of the CV cycle and the peak current at high electrode roughness. Thus, the shifting of oxidation onset should have originated from the reduction in ionization potential of SVA-FTM films due to a higher degree of molecular ordering compared to conventional-FTM films [139,140]. After estimating different electronic levels from UV-vis spectra and CV, we have summarised them in Figure 4.6 (f) to better visualize these systems.

### 4.3.Charge transport study

Finally, to explore how the chloroform vapor-assisted nano-structuration affects the anisotropic in-plane charge transport, parallel and perpendicular OFETs have been fabricated, as shown in the inset of Figure 4.6 (a). As bottom gate top contact (BGTC) device architecture offers lower contact resistance than its bottom gate bottom contact (BGBC) counterparts, [32] all the OFETs were fabricated in BGTC structure, where a smooth $SiO_2$ gate insulator provides the least damage to the dielectric/semiconductor interface. The output characteristics ($I_{DS} - V_{DS}$) and the transfer characteristics ($I_{DS} - V_{GS}$) for parallel and perpendicular OFETs are shown in Figure 4.6 (a-d), where a p-type unipolar behavior is evident for both type of the organic semiconducting thin films. Moreover, at each respective gate bias, around ~5 times (conventional FTM) and ~8 times (SVA-FTM) higher drain current is found in the parallel OFETs as compared to the perpendicular ones, evidencing the electrical anisotropy in charge transport. Although SVA-FTM films show a higher drain current, the hysteresis found in SVA-FTM films is also higher compared to the conventional FTM films. A higher degree of paracrystallinity and Urbach-type localized states inside the optical gap could be the reason for this higher hysteresis in output characteristics. Now, utilizing the equation (1) and a $W/L$ ratio of 50, the average effective hole mobility (parallel) for SVA-FTM film has been estimated to be 0.0498 $cm^2V^{-1}s^{-1}$ at $V_{DS} = -40\ V$ which is ~5 times higher compared to the conventional FTM films, 0.0109 $cm^2V^{-1}s^{-1}$. Further, from the Ohmic region of the output characteristic curves, the electrical conductivity ($\sigma$) of both films in parallel and perpendicular direction have been evaluated at 0 V and -40 V gate bias, using the following relation, [70,141]

$$\sigma = \frac{LI_{DS}}{WdV_{DS}} \tag{4.7}$$

Where the film thickness ($d$) has been taken to be 15 nm for conventional FTM films [124]

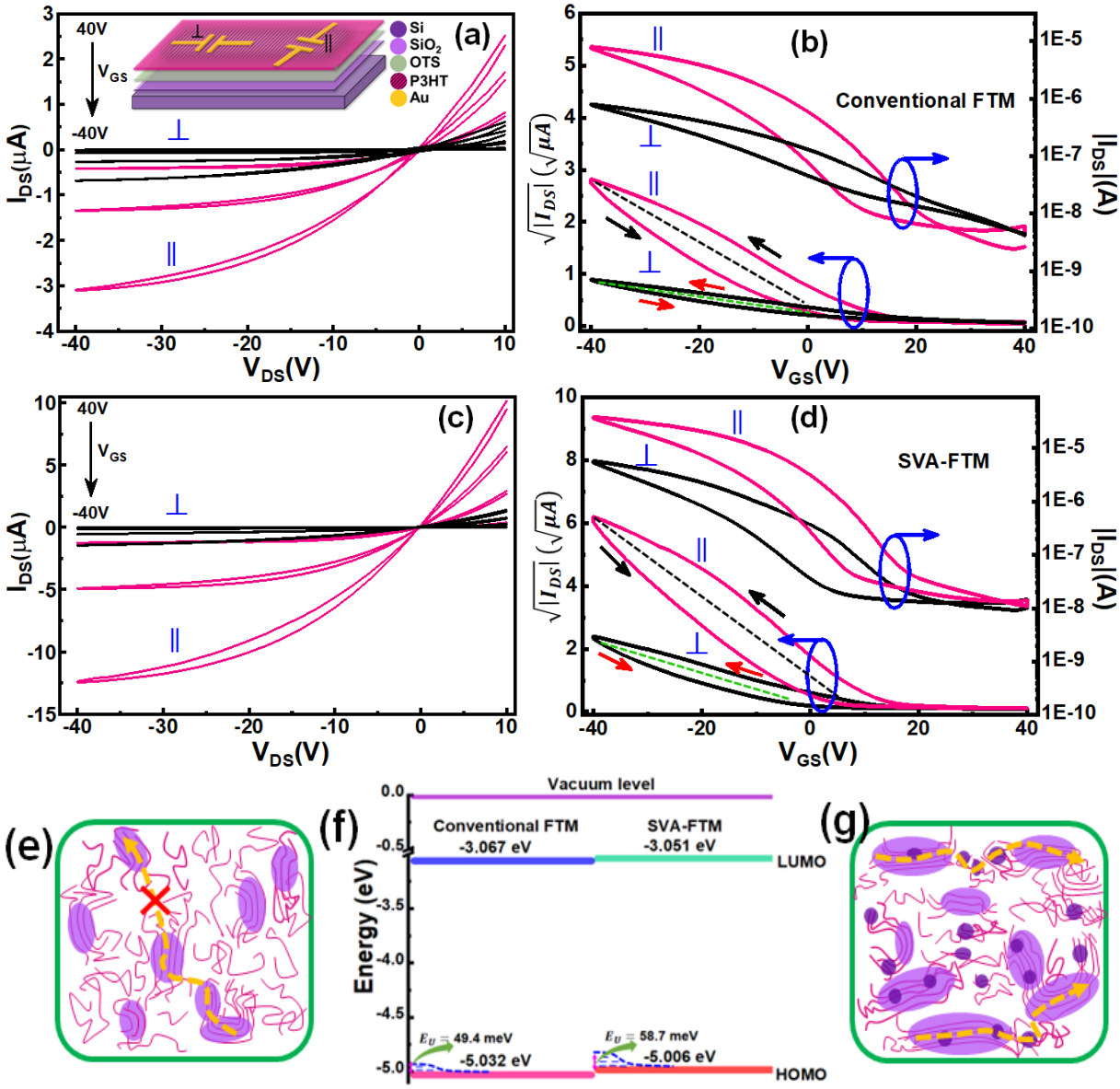


**Figure 4.6** shows output and transfer characteristics of P3HT films prepared by conventional FTM (a & b) and SVA-FTM (c & d), and (e) & (g) represents schematically charge transport pathways in conventional FTM and SVA-FTM films, respectively, and (f) shows electronic levels in both the films.

and 23 nm for SVA-FTM films (as estimated from the AFM step height measurement results, shown in Figure 4.2 (e)). It has been found that the conductivity also shows anisotropic behavior for both films and the $\sigma_{max}$ was observed along the polymer backbone direction, as per the TABLE 4.3. Pandey et al. [70] observed a similar kind of result in polymer/graphene oxide composites. Thus, much higher mobility and conductivity in the case of SVA-FTM films can be elucidated via the Mott variable-range hopping (VRH)

**TABLE 4.3** Electrical parameters estimated from the parallel and perpendicular OFETs.

| **Electrical parameters → Devices↓** | | **Mobility μ ($cm^2\ V^{-1}\ s^{-1}$)** | **Subthreshold swing (V/dec)** | **Trap density ($cm^{-2}$)** | $\frac{\mu_{\parallel}}{\mu_{\perp}}$ | $\frac{A_{\parallel}}{A_{\perp}}$ | **Conductivity, σ (S/cm)** | |
|---|---|---|---|---|---|---|---|---|
| | | | | | | | $V_{GS} = 0V$ | $V_{GS} = -40V$ |
| Conventional FTM film | ∥ | $(10.9\pm0.9)\times10^{-3}$ | 11.4 | $1.20\times10^{13}$ | 7.8 | 3.63 | $(7.06\times10^{-4})\pm6\%$ | $(26.14\times10^{-4})\pm9\%$ |
| | ⊥ | $(1.4\pm0.5)\times10^{-3}$ | 34.9 | $3.66\times10^{13}$ | | | $(1.45\times10^{-4})\pm16\%$ | $(3.23\times10^{-4})\pm14\%$ |
| SVA-FTM film | ∥ | $(49.8\pm3.8)\times10^{-3}$ | 9.86 | $1.03\times10^{13}$ | 5.4 | 1.42 | $(15.21\times10^{-4})\pm9\%$ | $(61.17\times10^{-4})\pm11\%$ |
| | ⊥ | $(9.3\pm1.0)\times10^{-3}$ | 12.9 | $1.35\times10^{13}$ | | | $(3.71\times10^{-4})\pm8\%$ | $(10.27\times10^{-4})\pm12\%$ |

mechanism, [142] which states that charge carriers can hop every now and then between localized states through multiple pathways. However, this hopping probability depends on the spatial and energetic difference between two localized states. In SVA-FTM films, HRTEM and XRD evidenced that there exist larger ordered domains and many quantum dot-like aggregated structures, which lower the effective hopping radius and form a network of interconnected conductive pathways. Thus, a chloroform vapor saturated environment assists the formation of such crystalline and oriented domains spanning the entire FTM film between source and drain, through which charge carriers can marginally percolate (schematically shown in Figure 4.6 (e) & (g)). However, the mobility anisotropy is found lower (~5) in SVA-FTM film compared to the conventional FTM one (~8), and this finding is in accordance with the optical anisotropy (***DR***). This lower mobility anisotropy in SVA-FTM films arises due to the enhancement in mobility along the perpendicular direction also because of the aggregated nanostructures. The effective density of interfacial traps ($N_{SS}^{max}$, calculated from the OFETs shown in Figure 4.6) also found lower in SVA-FTM films. Thus, the uniform distribution of aggregated nanostructures and higher conjugation length in SVA-FTM film tunes the HOMO level (and work function) in such a way that facilitates charge carrier injection/collection lowering the contact resistance ($R_c$).

### 4.4.Conclusions

In conclusion, we have successfully developed a facile thin film processing method utilizing the key advantages of conventional FTM and solvent vapor saturated atmosphere, which elucidated a path to fabricate homogeneous, highly anisotropic, and crystalline thin solid polymer films that can be transferred over desired substrates without disturbing any underlying layers coated on the substrate. Although the paracrystalline disorder along the (*h*00) direction and Urbach tail width were found comparatively higher in SVA-FTM films, lower exciton bandwidth, extended structural coherence, and conjugation length proved to dominate the local in-plane anisotropic charge transport. The 2D mapping system explored the homogeneity of the as-prepared films, while through AFM and KPFM, we explored the topographical evolution in film surface properties. Several quantum dots like aggregated nanostructures have been found homogeneously distributed over the ordered crystalline domains, as probed through HR-TEM, and the aggregation was found H-type, according to Spano's model. A lower FWHM and higher peak intensity in Raman spectra exemplified an extended and more compact π-orbital overlap in SVA-FTM films. Moreover, the oxidation onset potential in CV measurement also shifted to a lower value, indicating the tuning of HOMO-LUMO positions in SVA-FTM films. Finally, through parallel and perpendicular OFET measurement, we probed the charge transport anisotropy, and the maximum parallel charge carrier mobility was almost five times greater than the conventional ones. Thus, exploring several fundamental properties related to film quality, our study demonstrates a clear picture of structure-property correlation along with a cheap and facile route of thin film fabrication process, SVA-FTM, aiming towards solution-processed high-performing organic electronic devices.